NEUROSCIENCE

Australopithecus afarensis endocasts suggest ape-like brain organization and prolonged brain growth

Philipp Gunz[1]*†, Simon Neubauer[1]*, Dean Falk[2,3], Paul Tafforeau[4], Adeline Le Cabec[1,4], Tanya M. Smith[5], William H. Kimbel[6], Fred Spoor[1,7,8], Zeresenay Alemseged[9]

Human brains are three times larger, are organized differently, and mature for a longer period of time than those of our closest living relatives, the chimpanzees. Together, these characteristics are important for human cognition and social behavior, but their evolutionary origins remain unclear. To study brain growth and organization in the hominin species *Australopithecus afarensis* more than 3 million years ago, we scanned eight fossil crania using conventional and synchrotron computed tomography. We inferred key features of brain organization from endocranial imprints and explored the pattern of brain growth by combining new endocranial volume estimates with narrow age at death estimates for two infants. Contrary to previous claims, sulcal imprints reveal an ape-like brain organization and no features derived toward humans. A comparison of infant to adult endocranial volumes indicates protracted brain growth in *A. afarensis*, likely critical for the evolution of a long period of childhood learning in hominins.

INTRODUCTION

In contrast to African apes, the human brain growth pattern is characterized by high growth rates and protracted duration (*1*–*3*). Modern humans also give birth to relatively immature offspring who depend on caregivers for a long period of time (*4*–*6*). This provides a longer interval for cognitive development (*4*) and is believed to enhance the impact of postnatal experiences on neural connectivity (*7*). Another key difference between the brains of apes and humans involves the parietal and occipital lobes (*8*, *9*). In all apes, a well-defined lunate sulcus approximates the rostral (anterior) boundary of the primary visual cortex (Brodmann's area 17) of the occipital lobes (fig. S1). Some have argued that structural changes of the brain resulted in a more posterior (human-like) placement of the lunate sulcus on endocasts of australopiths and eventually to the disappearance of a clear endocranial impression in humans (*10*). Hypothetically, such brain reorganization could have been linked to behaviors that were more complex than those of their great ape relatives (e.g., tool manufacture, mentalizing, and vocal communication) (*9*). Unfortunately, however, the lunate sulcus typically does not reproduce well on endocranial imprints, so there is uncertainty about its position in australopiths. There is debate whether protracted brain growth and reorganization are merely by-products of the brain size increase in the genus *Homo* beginning by 2 million years (Ma) ago or evolved in the genus *Australopithecus* roughly 1 Ma before the marked expansion of the brain (*2*, *6*, *11*–*14*). *Australopithecus afarensis*, a species of hominins inhabiting eastern Africa more than 3 Ma ago, occupies a key position in hominin phylogeny, as it is potentially ancestral to all later hominins, including the *Homo* lineage. Previous studies of the endocranial growth pattern in *A. afarensis* were hampered by postmortem fracturing, displacement, and plastic deformation of the fossilized cranial bones, as well as uncertainties about the age at death of infant individuals. On the basis of conventional and synchrotron high-resolution computed tomography (CT) scans of original fossils from the Ethiopian sites Dikika and Hadar, we used virtual reconstruction techniques to correct for damage in two well-preserved *A. afarensis* infant crania (DIK-1-1 from Dikika and A.L. 333-105 from Hadar; Fig. 1) and six adults [A.L. 162-28, A.L. 288-1 ("Lucy"), A.L. 333-45, A.L. 417-1, A.L. 444-2, and A.L. 822-1; Fig. 2 and fig. S2]. We created virtual endocranial imprints to study brain organization in *A. afarensis*, estimated the age at death for the two infant specimens, and used geometric morphometric methods to estimate endocranial volumes (EVs). These data shed new light on two questions that have been controversial: (i) Is there evidence for human-like brain reorganization in *A. afarensis*? (ii) Was the pattern of brain growth in *A. afarensis* more similar to that of chimpanzees or that of humans?

RESULTS

Ape-like brain organization

The DIK-1-1 braincase is filled with fine-grained sandstone matrix, creating a natural endocast (Fig. 3 and fig. S3). The synchrotron microtomographic images reveal exceptional preservation of the internal aspects of the cranial base. Even the delicate bones of the anterior cranial fossa are preserved, including displaced but undistorted fragments of the orbital roof. The beautifully preserved endocast of DIK-1-1 has an unambiguous impression of a lunate sulcus in an anterior (ape-like) position (Fig. 3 and fig. S3), even after correction for taphonomic distortion (fig. S4A). The identification of the surrounding sulcal impressions on the parietal and occipital lobe corroborates this assessment. The micro-CT scans also reveal previously undetected sulcal impressions on the partial cranium A.L. 162-28 from Hadar (Fig. 4 and fig. S5), thereby resolving a long-standing debate (*13*, *15*–*17*) about the position of the lunate sulcus in this specimen. Central to this discussion are the identification of the intraparietal sulcus (ip), its relative position to other sulcal impressions, and the orientation of the specimen. A comparison of A.L. 162-28, which only preserves part of the parietal and occipital bones, to the

[1]Department of Human Evolution, Max Planck Institute for Evolutionary Anthropology, Deutscher Platz 6, Leipzig 04103, Germany. [2]Department of Anthropology, Florida State University, Tallahassee, FL 32310, USA. [3]School for Advanced Research, 660 Garcia St., Santa Fe, NM 87505, USA. [4]European Synchotron Radiation Facility, 71 Avenue des Martyrs, CS-40220, F-38043, Grenoble cedex 09, France. [5]Australian Research Centre for Human Evolution, Griffith University, 170 Kessels Rd., Nathan 4111, Queensland, Australia. [6]Institute of Human Origins, and School of Human Evolution and Social Change, Arizona State University, Tempe, AZ 85287, USA. [7]Centre for Human Evolution Research, Department of Earth Sciences, Natural History Museum, London SW7 5BD, UK. [8]Department of Anthropology, UCL, London WC1H 0BW, UK. [9]Department of Organismal Biology and Anatomy, University of Chicago, Chicago, IL 60637, USA.
*These authors contributed equally to this work.
†Corresponding author. Email: gunz@eva.mpg.de

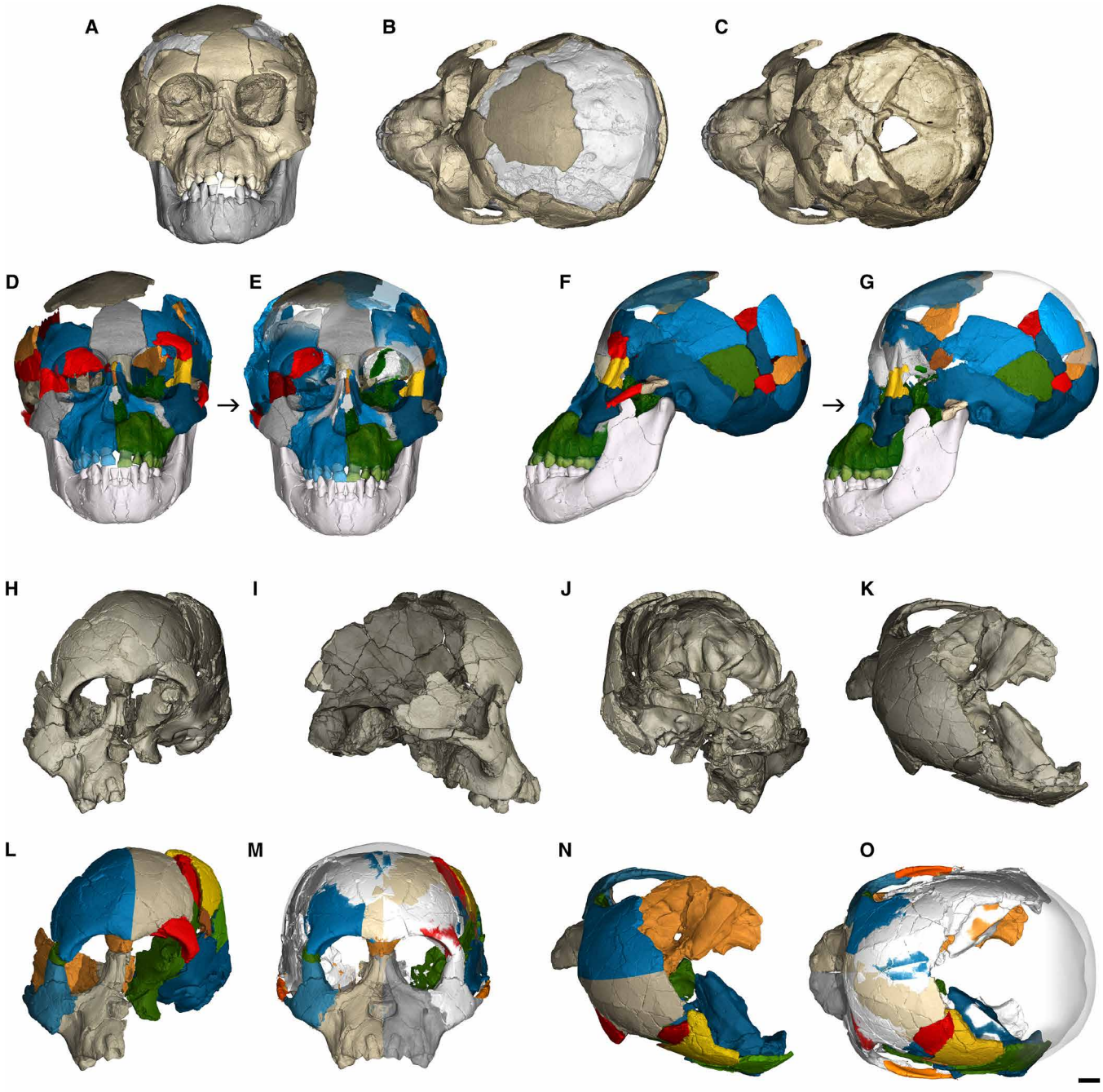

Fig. 1. Virtual reconstruction of *Australopithecus afarensis* infants from Dikika and Hadar. DIK-1-1 (**A** to **G**) and A.L. 333-105 (**H** to **O**) as preserved and reconstructed. (A) Frontal view. (B) Superior view. (C) Manual segmentation of the endocranial matrix reveals exceptional preservation of the endocranial cavity. (D to G) 3D models of the DIK-1-1 skull before (D and F) and after (E and G) virtual reconstruction in frontal and left lateral view. (H to K) Scan of the original A.L. 333-105 fossil specimen. (L) Manual segmentation. (M to O) Virtual reconstruction. The reconstructed outer shells of the braincases are shown as semitransparent surfaces. Scale bar, 1 cm.

more complete fossil crania that were recovered more recently from the same site (Fig. 4, A and B) confirms that Holloway's original orientation of the specimen was correct [(*13*, *16*) contra (*15*, *17*)]. The micro-CT data reveal clear, previously undetected impressions of unambiguously ape-like lunate sulci [(*15*, *17*) contra (*13*, *16*)] on the left and right side (Fig. 4, C and D, and fig. S5). What had previously (*15*–*17*) been identified as the intraparietal sulcus (ip) is an impression of the lateral calcarine sulcus (lc) on the occipital lobe. The feature previously incorrectly identified as a possible lunate sulcus impression is related to the remnants of the fused lambdoidal suture and the occipital inferior sulcus (occi). Similar impressions can be seen in the chimpanzee endocranium shown in Fig. 4F. The relevant morphology is not sufficiently preserved to identify the lunate sulcus conclusively in the other individuals studied here, but an impression

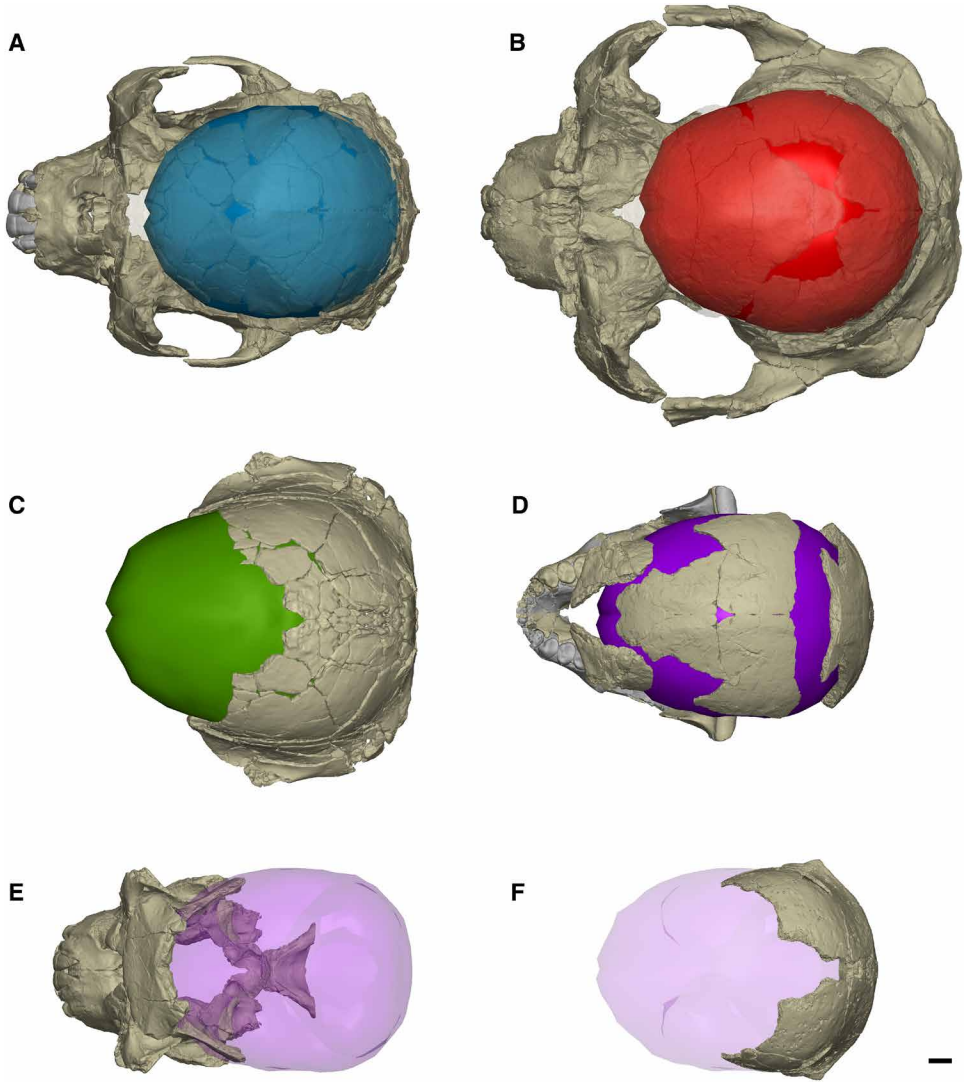

Fig. 2. Virtual reconstructions of *A. afarensis* adults. (**A**) Reconstruction of A.L. 822-1 in superior view. One of the 122 thin-plate spline (TPS)–based reconstructions of the endocast is shown in blue. (**B**) A.L. 444-2; a TPS estimation of the endocranial surface is shown in red. (**C**) A.L. 333-45; endocast in green. This endocranial reconstruction was created by scaling the endocranial surface of 444-2 based on landmarks and semilandmarks on the available morphology. (**D**) A.L. 288-1 (Lucy); endocast in purple (TPS estimation). (**E**) A.L. 417-1; the endocast of A.L. 288-1 is shown as a semitransparent surface. (**F**) A.L. 162-28; the endocast of A.L. 288-1 is shown as a semitransparent purple surface for size comparison. Scale bar, 1 cm.

posterior to the left superior temporal sulcus in A.L. 333-105 is consistent with the most lateral part of an ape-like expression (fig. S6).

Both *A. afarensis* infants preserve detailed sulcal impressions in the frontal lobe. As in other australopiths, a middle frontal sulcus (fm) runs parallel to the superior frontal sulcus (fs). On A.L. 333-105, a distinct inferior frontal sulcus (fi) also runs parallel to fs and fm (fig. S6). A recent study overturned the notion that this frontal lobe configuration is derived compared to apes, as the same sulcal configuration can also be found in some chimpanzees (*18*). Neither DIK-1-1 nor A.L. 333-105 exhibits the incipient reorganization of the inferior frontal gyrus recently described in *Homo naledi* (*19*). Overall, the endocasts of DIK-1-1, A.L. 162-28, and A.L. 333-105 indicate an ape-like brain organization in *A. afarensis*. Contrary to previous claims (*10*, *20*), we find no unambiguous indication of brain reorganization in any *A. afarensis* endocast that preserves detailed sulcal impressions.

Estimating EV

We used multivariate statistics based on detailed measurements of the endocranial surface in apes ($N = 122$) to estimate EV in the best-preserved *A. afarensis* fossil crania (Figs. 1 and 2 and Table 1). The unreconstructed virtual endocast of DIK-1-1 has an EV of 237 ml. After correcting for displacements (Fig. 1G), the EV of DIK-1-1 is 275 ml (SD, 1 ml; range, 273 to 277 ml). The A.L. 333-105 infant cranium from Hadar is slightly larger than DIK-1-1: Multiple reconstructions yield EVs between 310 and 317 ml. Taking into account the reconstruction uncertainty, estimates of adult EV in *A. afarensis* yield an average of 445 ml (SD, 60 ml; range, 365 to 526 ml) based on the reconstruction distributions of the following fossil specimens: A.L. 288-1 (mean EV, 388 ml; SD, 9 ml; range, 365 to 417 ml), A.L. 822-1 (mean EV, 382 ml; SD, 4 ml; range, 374 to 392 ml), A.L. 333-45 (mean EV, 488; SD, 1 ml; range, 486 to 492 ml), and A.L. 444-2 (mean EV, 522 ml; SD 1 ml; range, 519 to 526 ml). Our volumetric estimates for

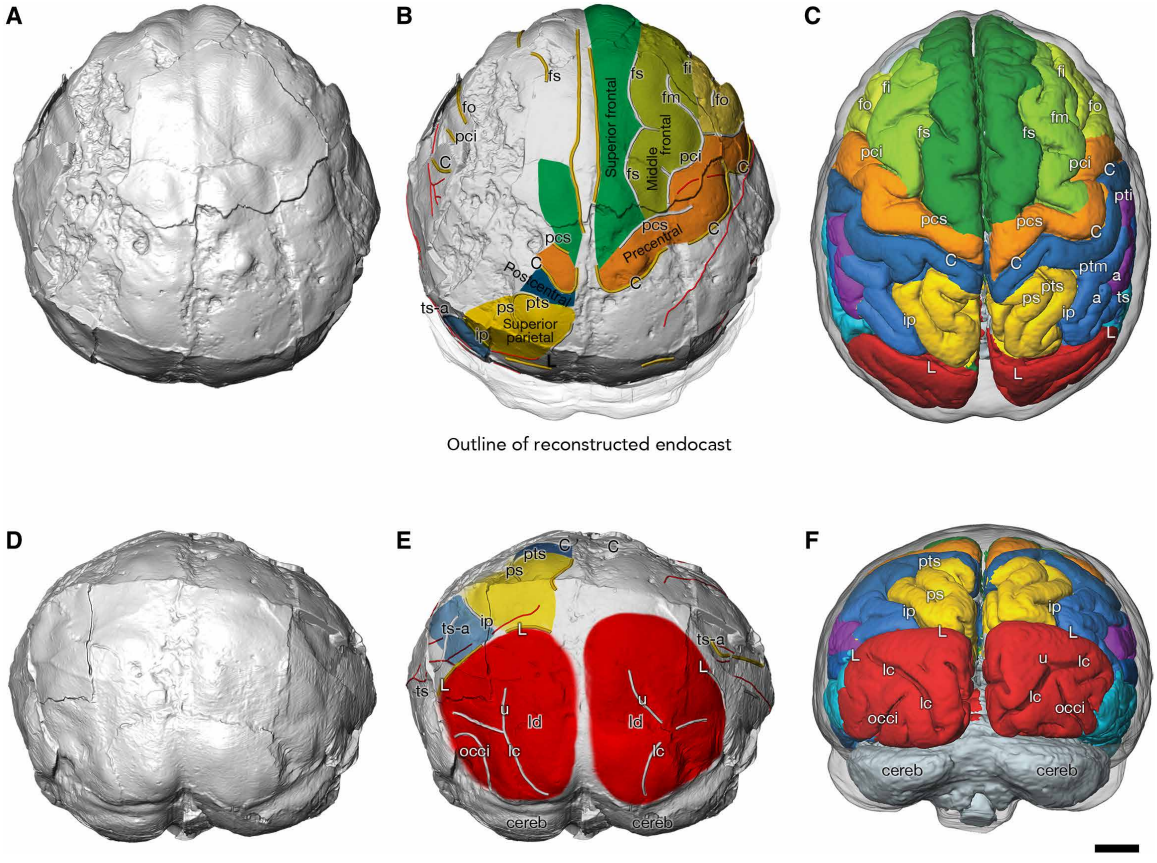

Fig. 3. Endocranial morphology of DIK-1-1. Virtual endocast in superior (**A** and **B**) and posterior view (**D** and **E**). Comparison of the endocranial surface with a juvenile chimpanzee brain (**C** and **F**) [3D model built from magnetic resonance images (MRIs)] illustrates the overall ape-like brain organization of the DIK-1-1 endocast, including an anteriorly placed lunate sulcus (L). Gyri are color-coded; sulci are labeled as in (C) and (F). Meningeal vessel impressions are shown in red. C, sulcus centralis; fs, frontalis superior; fm, frontalis medius; fi, frontalis inferior; fo, fronto-orbitalis; h, horizontal ramus of pci; ip, s. intraparietalis; pci, praecentralis inferior; pcs, praecentralis superior; ps, parietalis superior; pti, postcentralis inferior; ptm, postcentralis medius; pts, postcentralis superior; L, s. lunatus; ts, temporalis superior; ts-a, ramus temporalis superior; tm, temporalis medius; occi, occipitalis inferior; lc, s. calcarinus lateralis; u, s. calcarinus ramus superior; cereb, cerebellum; ld, lambdoidal suture. Scale bar, 1 cm.

the Hadar endocasts are very similar to those derived by traditional endocast reconstruction methods by Holloway *et al.* (*10*) and Kimbel and Rak (*21*), which we interpret as validation of our morphometric reconstructions and results. The partial crania A.L. 162-28 and A.L. 417-1 are not complete enough for reliable EV estimations, but a comparison with the reconstructed *A. afarensis* adults (Fig. 2) demonstrates that they are most similar to A.L. 288-1 (Lucy) and A.L. 822-1 and therefore likely had EVs on the lower end of the known *A. afarensis* range.

Age at death of DIK-1-1 and A.L. 333-105

A comparison of the calcification of DIK-1-1's permanent mandibular teeth to those of known-age chimpanzees yields a chimpanzee-equivalent age of 2.1 (range, 2.05 to 2.21) years. The propagation phase-contrast synchrotron microtomographic data of DIK-1-1 made it possible to determine the specimen's actual age at death using virtual histology protocols (*22*). Internal accentuated lines in the first molar were matched to the canine, yielding an age of 2.4 years (Fig. 5A), which is markedly younger than human calcification standards but similar to chimpanzees (fig. S7). This pattern of dental development is consistent with other australopiths (*23*). The first molar metaconid of DIK-1-1 formed in 603 days, which is at the low end of the range for chimpanzees and shorter than in other fossil hominins, modern humans, or gorillas (table S1). On the basis of these data, our best estimate of age at death for DIK-1-1 is 2 years and 5 months, which is younger than a previous estimate of ~3 years (*11*). The upper dentition of A.L. 333-105 is developmentally equivalent to the upper dentition of DIK-1-1, suggesting that this specimen died at similar age (fig. S8).

Comparing endocranial growth curves

Endocranial growth curves computed from a large cross-sectional ontogenetic series of modern humans (N = 1275) and chimpanzees (N = 337) reveal clear species differences in absolute growth rates (Fig. 5B). The EVs of the two *A. afarensis* infants fall within the lower half of the chimpanzee range of variation. The average adult EV of *A. afarensis* (445 ml; SD, 60 ml) is larger than in *Pan troglodytes* (369 ml; SD, 37 ml; N = 240). We also computed a relative EV (rEV) for all extant and fossil subadults as the ratio between EV and the adult mean EV of this species. While there is some overlap between the rEV values of chimpanzees and humans, the average trajectories reveal species differences in the pattern of brain growth (Fig. 5, C to E). Using permutation techniques, we computed rEVs for *A. afarensis* taking into account the reconstruction uncertainties of EV relative to chimpanzees, the uncertainty regarding the age at death, and the

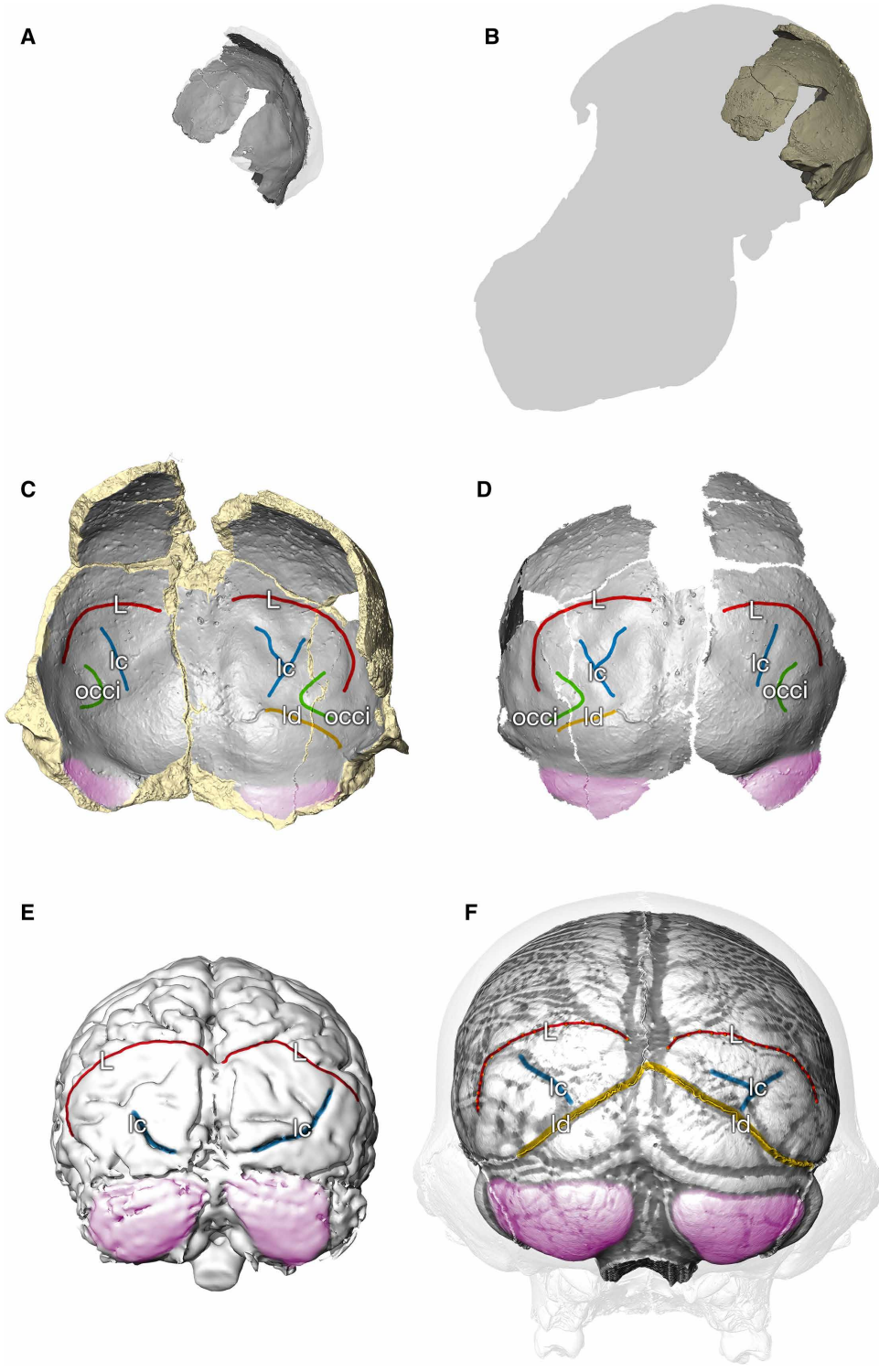

Fig. 4. Endocranial morphology of A.L. 162-28. (**A**) Comparison of the partial cranium A.L. 162-28 with the reconstructed skull A.L. 822-1 (**B**). (**C**) Anterior view of A.L. 162-28. The micro-CT data reveal a previously undetected impression of a lunate sulcus (L; red) on the left and right side. What had previously been identified as the intraparietal sulcus (ip) is an impression of the lateral calcarine sulcus (lc) on the occipital lobe. The feature previously incorrectly identified as a possible human-like lunate sulcus impression is related to the remnants of the fused lambdoidal suture (ld; yellow) and the occipital inferior sulcus (occi; green). (**D**) Posterior view of the endocranial surface of A.L. 162-28. (**E**) Posterior view of a chimpanzee brain based on an in vivo MRI scan ("Amanda" from the Yerkes National Primate Research Center). (**F**) Chimpanzee endocast based on a postmortem CT scan (*P. troglodytes verus* from the Taï forest). We superimposed a grayscale gradient based on the local curvature to visually enhance the sulcal impressions.

Table 1. *A. afarensis* EVs. The means and SDs are based on the distribution of reconstructions (i.e., on the hundreds of individual estimates).

Specimen	Age	EV mean (ml)	SD	Min	Max	Method
DIK-1-1	2.4 years	275	1	273	277	TPS estimation
A.L. 333-105	2.2–2.4 years	313.5	3	310	317	TPS estimation
A.L. 822-1	Adult	382	4	374	392	TPS estimation
A.L. 288-1	Adult	388	9	365	417	TPS estimation + scaling of A.L. 822-1
A.L. 333-45	Adult	488	1	486	492	Scaling of A.L. 444-2
A.L. 444-2	Adult	522	1	519	526	TPS estimation
Adult *A. afarensis*		445	60	365	526	

adult range of *A. afarensis* EVs. On average (Fig. 5C), and when considered individually (Fig. 5, D and E), the rEVs based on DIK-1-1 and A.L. 333-105 indicate prolonged brain growth in *A. afarensis*, in that it takes longer for individuals to reach their adult EVs. This confirms previous studies (*2*, *11*) and remains true when the relatively large EV of A.L. 444-2 is removed from the computation. Our findings therefore suggest that brain growth in *A. afarensis* was protracted as in modern humans. What distinguishes modern humans from *A. afarensis* and chimpanzees (*24*) is a combination of high growth rates (Fig. 5B) and prolonged brain growth (Fig. 5, C to E).

DISCUSSION

Prolonged brain growth and maturation have often been viewed as a consequence of evolutionary brain size increase in the genus *Homo*: a shift in life history required to evolve large adult brains despite obstetric constraints related to upright walking (*25*). In contrast to this view, our data from *A. afarensis* demonstrate that prolonged brain growth is not a mere by-product of evolutionary brain size increase. One can predict the average neonatal brain size in *A. afarensis* based on the statistical relationship between the brain size of newborns and adults in anthropoids (*26*). The pelvic dimensions of the small, presumed female *A. afarensis* specimen A.L. 288-1 (Lucy) suggest that it would have been possible to give birth to such a predicted *A. afarensis* neonate, potentially requiring some rotation of the fetus during parturition (*26*–*28*). Our findings therefore challenge the central tenet of the obstetric dilemma hypothesis (*25*) and suggest that obstetric constraints are not the proximate cause of the origins of prolonged brain growth in hominins. This view is in line with an earlier study that emphasized the importance of energetic constraints of the maternal metabolism on fetal growth and gestation length, suggesting that the evolution of altriciality in hominins had little to do with pelvic morphology (*29*).

The evidence from virtual dental histology shows that the dental development of DIK-1-1 was broadly comparable to that of *P. troglodytes* and therefore faster than in modern humans, whereas the same individual's small rEV suggests a prolonged period of brain development relative to chimpanzees. This indicates that the developmental pace of teeth and brain need not always be synchronized and can evolve independently, at least to some degree. The fact that protracted brain growth emerged in hominins as early as 3.3 Ma ago could suggest that it characterized all of subsequent hominin evolutionary history. However, it is possible that patterns of brain development varied among hominins and did not follow a linear evolutionary trajectory toward the modern human condition (*5*). Among primates in general, different rates of postnatal growth and maturation are associated with different infant-care strategies (*30*), suggesting that the extended period of brain growth in *A. afarensis* may have been linked to a long dependence on caregivers (*24*, *31*). Alternatively, slow brain growth could also primarily represent an energetic adaptation, e.g., to less productive environments, by spreading the energetic requirements of dependent offspring over many years. In either case, the protracted brain growth in *A. afarensis* provided a basis for subsequent evolution of the brain and social behavior in hominins and was likely critical for the evolution of a long period of childhood learning.

MATERIALS AND METHODS

CT scanning of *A. afarensis* fossils

Our analyses are based on high-resolution conventional and synchrotron CT scans of original fossils from Dikika (*11*) and Hadar (*21*, *32*–*34*) in Ethiopia. We used virtual reconstruction techniques (*35*) to correct for damage in DIK-1-1, A.L. 333-105, A.L. 162-28, A.L. 288-1 (Lucy), A.L. 333-45, A.L. 417-1, A.L. 444-2, and A.L. 822-1. When the DIK-1-1 specimen was reported originally (*11*), the skull was still partially covered in sandstone matrix and attached to many axial elements of the thorax. Following extensive additional preparation at the National Museum of Ethiopia (Addis Ababa) to isolate the various elements, the cranium and mandible were first imaged on the ID17 beamline at the European Synchrotron Radiation Facility (ESRF) in Grenoble, France. The procedure involved single-distance propagation phase-contrast x-ray synchrotron microtomography, using a specific absorption control protocol to improve data quality when scanning large fossils with a monochromatic beam (*36*). These data used for the skull reconstruction were collected with an isotropic voxel size of 45.7 μm. For more detailed studies on dental development, DIK-1-1 was also scanned on the ID19 beamline. The acquisition parameters are presented in table S2. The fossils from Hadar, Ethiopia (accession number A.L.), were scanned at the National Museum of Ethiopia using the portable SkyScan 1173 micro-CT of the Max Planck Institute for Evolutionary Anthropology (Leipzig, Germany).

Dental calcification scoring scale for microtomographic slices

Assessing the degree of tooth calcification can provide valuable information when interpreting the biology of extinct juvenile primates. However, incomplete mineralization can substantially reduce the contrast of the dental germs on radiographs, even if the original density pattern is preserved. In studies of extant species, it was found

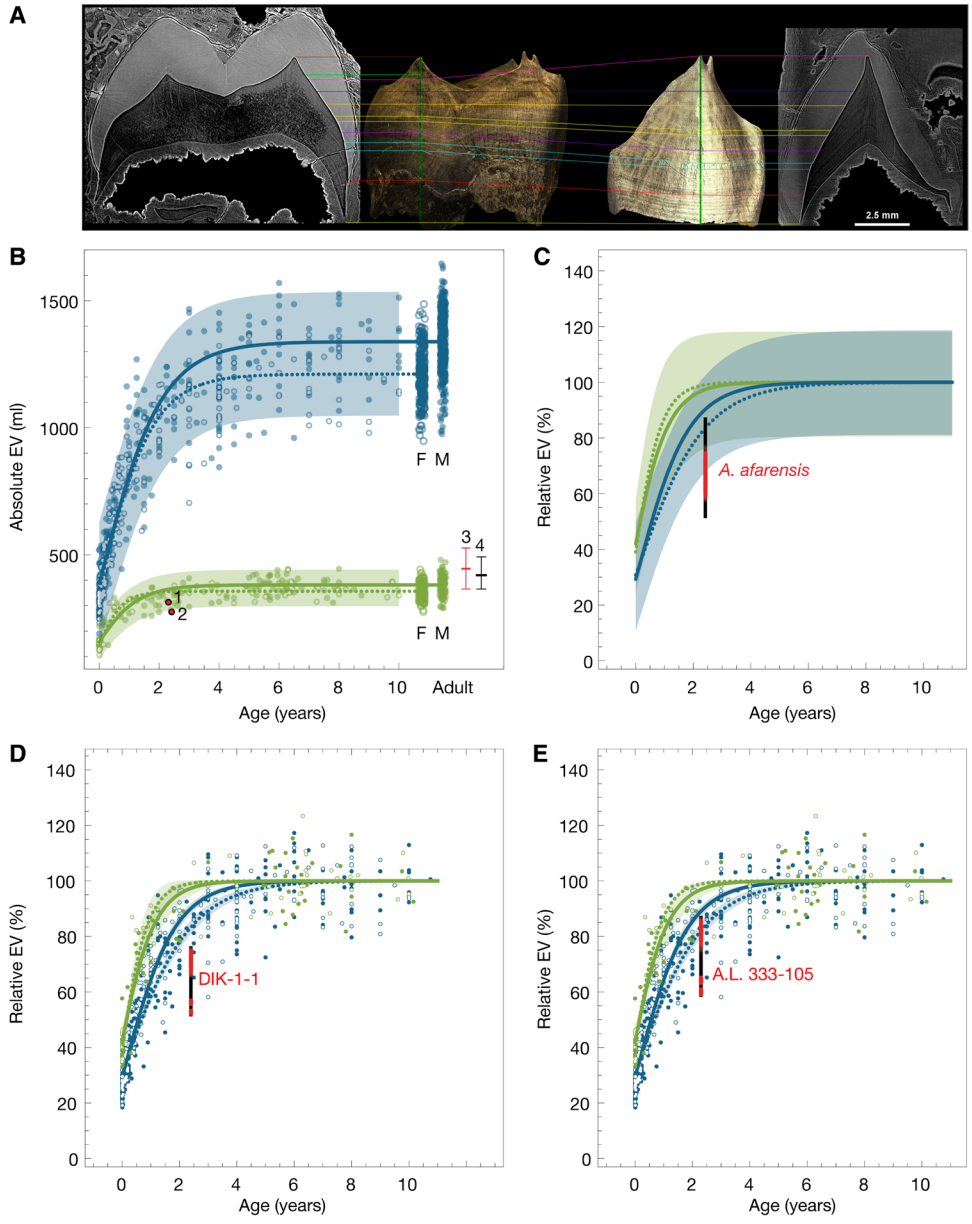

Fig. 5. Age at death and endocranial growth curves. (**A**) Matching of DIK-1-1's permanent right lower first molar and LUC for age at death determination using synchrotron virtual dental histology. The age at death is the summation of the initiation age (9 days), cuspal enamel formation time (228 days), and lateral enamel (624 days) in the canine: 861 days (2.4 years). (**B**) Absolute EV in the first 10 years of life in modern humans, chimpanzees, and *A. afarensis*. 1, A.L. 333-105; 2, DIK-1-1; 3, *A. afarensis* adult mean and range; 4, *A. afarensis* adult mean and range without A.L. 444-2; F, female; M, male. Average growth patterns are visualized using Gompertz curves for males and females (open circles and dotted line) separately; 95% single prediction bands based on the pooled sample. (**C**) Relative growth curves based on the ratio between EV and the adult mean EV (rEV) for modern humans and chimpanzees, split by sex. (**D** and **E**) As in (C), but the infants DIK-1-1 and A.L. 333-105 are compared against individual *A. afarensis* adults. The rEVs of the *A. afarensis* infants indicate protracted brain growth, in that it takes *A. afarensis* individuals longer than chimpanzees to reach their adult EVs.

that dental calcification scores derived from virtual two-dimensional (2D) microtomographic slices were consistently higher than those based on conventional radiographs (*37*). Immature enamel and very thin dentine extensions are not visible in radiographs but can be observed in microtomographic slices. The latter allows more accuracy and precision than scoring radiographs, as there is no superimposition of structures and finer details can be observed. When scoring fossils, additional error can be introduced by increased mineralization of immature enamel matrix due to diagenetic substitution, erroneously suggesting more advanced maturation. When using virtual slices, these errors can be identified by observations of the shape of the enamel at the cervix and the onset of root development.

Given the above complications with the conventional approach to scoring tooth calcification, we developed a new method for extant and extinct primates. As in the previous approach, discrete dental stages are identified, but this is done using normalized virtual slices of the dental germs following the "developmental planes" as defined in (*37*). We assess tooth morphology visible in slices with a voxel size of 40 μm or less and explicitly without any reference to the degree of mineralization. The latter enables analysis of fossil specimens with

the same accuracy as modern samples as long as the outline of developing tooth germs is visible.

The new scoring scale uses similar dental development milestones as in conventional radiographic assessments (*38*) but with more refined stages. Fifteen stages are defined. Each stage represents a threshold, and the associated score is given when all conditions are fulfilled in addition to the ones in the preceding stage. When a single definition is given, it applies to all types of teeth. When two definitions are given, the first one applies to single cusped/rooted teeth (S); the second one applies to multi-cusped/rooted teeth (M).

Score	Definition for µCT virtual sections
0.0	S/M: No visible crypt.
0.5	S/M: Crypt present, but no cusp tip visible.
1.0	S/M: First cusp tip present, but very small.
1.5	S: Cusp tip clearly visible, but no significant amount of cuspal enamel yet. M: Partial fusion of the cusps except for those with late initiation (e.g., hypocone of molars or paracone of premolars).
2.0	S: Clear extension of the cusp; clear deposition of cuspal enamel. M: Complete fusion of the cusps with just a thin, blade-like connection at the junction.
2.5	S: At least half of the cuspal enamel deposited; no lateral enamel yet. M: At least half of the cuspal enamel deposited at the junction between cusps.
3.0	S/M: Cuspal enamel finished, including occlusal surface, lateral enamel extension starting.
3.5	S/M: At least half of the lateral enamel already secreted.
4.0	S/M: Completion of the crown on one side; beginning of root extension, on at least one side.
4.5	S/M: Root extension on both sides; root length clearly shorter than crown height.
5.0	S: Root length slightly shorter than crown height. M: Beginning of root furcation.
5.5	S: Root length equal to crown height. M: Clear root furcation.
6.0	S: Root length clearly larger than crown height; root extension is not yet finished. M: Complete root furcation; root extension is not yet finished.
7.0	S/M: Root extension nearly complete, but apical aperture still larger than root canal.
8.0	S/M: Root apex complete; apical aperture equal or smaller than the root canal.

Chimpanzee-equivalent age at death determination

Kuykendall developed a regression model to estimate calendar age from the radiographic developmental scores of lower teeth of known-age chimpanzees (*38*). Although this may not be applicable to other taxa to estimate calendar ages, it does facilitate comparisons between different taxa using "chimpanzee-equivalent ages" as long as their general dental pattern is roughly similar to that of chimpanzees. However, this regression model cannot be applied directly to microtomographic slices given the methodological concerns outlined above. We created a conversion scale by comparing the scoring of lower permanent teeth of juvenile chimpanzees and humans using both the Kuykendall approach based on radiographs and our new method based on standardized virtual sections (data file S1: sheets 1 to 3). We also assessed whether enamel thickness has an impact on the conversion between the two methods. This was found to be the case for stages 2.0 and 2.5 only, when most of the cuspal enamel is deposited. Given these differences, two conversion models were derived: one for thin or moderately thick enamel and one for thick enamel (data file S1: sheet 2). The difference between these two models is small and does not lead to substantial errors in most cases.

Scoring the dental development of DIK-1-1 and A.L. 333-105

The development of the permanent teeth of DIK-1-1 (save for M3s, which had not yet initiated at the time of death) was scored based on synchrotron microtomographic images with a voxel size of 30.3 µm (data file S1: sheets 4 and 5). The development of the left I^1 to M^1 of A.L. 333-105 (data file S1: sheet 6) was scored based on conventional microtomographic data (SkyScan 1173; 35.5 µm voxel size). The conversion scale with the thick enamel model was used to obtain a chimpanzee-equivalent age for DIK-1-1 using its lower teeth. Because the Kuykendall regression does not include upper teeth, we also applied the scoring method to the upper teeth of DIK-1-1 and A.L. 333-105 to compare the relative developmental levels of these two individuals (fig. S8). The lower teeth of DIK-1-1 gave a total score of 22.9 (average of 4 observers; range, 22.5 to 23.0) converted to a radiographic score of 19.0 ± 0.5. Application of the Kuykendall regression gives a chimpanzee-equivalent age of 2.13 years (2.05 to 2.21) for DIK-1-1. This age is a chimpanzee-referenced relative developmental age rather than an actual age at death. The latter can only be derived from dental histology, as discussed below. The upper dentition of DIK-1-1 differs slightly from the lower teeth by a more advanced P^3 and less advanced M^2, but the total dental score based on slices is very similar, with an average of 22.6 (22.5 to 23.0), which converts to 19.3 ± 1.0 for radiographic scoring. The upper dentition of A.L. 333-105 is developmentally very similar to the upper dentition of DIK-1-1. Its M^2 is missing, but with a plausibly inferred stage 2.0 or 2.5, the total slice scoring is 22.5 (average of 4 observers; range, 22 to 23), which corresponds to 19.25 (range, 19 to 20) for radiographic scoring. It implies that this specimen was either the same age or slightly younger than DIK-1-1. In A.L. 333-105, the dental crowns are overall larger than in DIK-1-1; however, its canine is less developed than in DIK-1-1 and still lacks a lingual cingulum (fig. S8A).

Synchrotron virtual dental histology: Age at death and crown formation time of DIK-1-1

The age at death of DIK-1-1 was determined through several steps. The neonatal (birth) line in the right lower first molar (RM_1) was found in the enamel 100 µm above the dentine horn of the metaconid, extending 980 µm from the dentin horn down the enamel-dentine junction (EDJ). Prenatal formation time was estimated by dividing this enamel thickness by the published rate of 3.31 µm/day for inner cuspal enamel secretion in *A. afarensis* (*39*) to yield 30 days of prenatal development and an initial extension rate of 32.7 µm/day. The EDJ of the RM_1 was then matched to the EDJ of the left upper canine (LUC) (Fig. 5A, pink line) following methods in (*22*). The LUC was determined to have initiated 290 µm after the neonatal line on the RM_1 EDJ, which was estimated at 9 days of age (290 µm/32.7 µm/day). The cuspal enamel formation time of the LUC was estimated by dividing the cuspal enamel thickness (1050 µm) by the published average cuspal enamel secretion rate of 4.60 µm/day in *A. afarensis* (*39*), yielding a cuspal formation time of 228 days. The lateral enamel

formation time of the LUC was determined by multiplying the long-period line periodicity (8 days) by the number of long-period Retzius lines formed before death (78 lines), yielding a formation time of 624 days. Thus, the age at death is the summation of the initiation age (9 days), cuspal enamel formation time (228 days), and lateral enamel (624 days) in the canine: 861 days (2.4 years).

The RM_1 metaconid formation time was also determined through several steps. The end of metaconid crown formation was matched to a developmental disruption in the LUC (Fig. 5A, red line). The number of subsequent long-period Retzius lines formed in the LUC was counted (*36*) and multiplied by the long-period line periodicity (*8*) to yield 288 days of RM_1 metaconid root formation. This was subtracted from the age at death (861 days), and the prenatal enamel formation time (30 days) was added, yielding a metaconid formation time of 603 days.

Segmentation of the endocasts

The endocranial cavity of DIK-1-1 is filled with a fine-grained sandstone matrix that creates a natural endocast. We first segmented this endocranial matrix manually using the software packages Avizo (Thermo Fisher Scientific) and VGSTUDIO MAX (Volume Graphics). A fragment of the frontal bone and a fragment of the left parietal were found separately and reattached to the skull (*11*). As these two bone fragments preserve even better endocranial surface detail than the natural endocast, we segmented the thin layer of air and adhesive between the natural endocast and the inner bone table and added it to the natural endocast. The borders of these "elevated" areas are visible as steps on the endocast, e.g., in Fig. 3 and fig. S3.

Reconstruction of the DIK-1-1 skull

For the virtual reconstruction of the DIK-1-1 skull, we separated matrix from bones (Fig. 1C) and isolated individual bone fragments along cracks (Fig. 1D). These virtual pieces were repositioned on the basis of anatomical criteria and bilateral symmetry (Fig. 1, E and G) following established protocols (*35*, *40*) using Avizo, VGSTUDIO MAX, and Geomagic (3D Systems).

Most cranial bones are well preserved, except parts of the sphenoid bone. Large portions of the parietal bones are missing (Fig. 1). Plastic deformation is minimal. Most bone fragments are merely displaced. In frontal view, the entire lower face—with the exception of the right zygomatic bone—is displaced: The left zygomatic bone has been pushed toward the midline, and the frontal process of the left zygomatic and the zygomatic process of the left temporal bone are both distorted. Both orbits are damaged, but the morphology on the right side is better preserved. The lateral part of the left supraorbital torus is crushed and shifted upward; on the right side, the area near the zygomaticofrontal suture is damaged.

The face of DIK-1-1 is displaced relative to the braincase; in lateral view, the lower face is tilted upward (Fig. 1F). When upper and lower teeth are brought into occlusion, a large gap exists between the mandibular condyles and the mandibular fossae. The nasal region is complete and undistorted but displaced laterally along with the frontal process of the left and right maxillary bones. In inferior view, the right side of the occipital bone and the basioccipital are pushed into the braincase (Fig. 1C). The posterior part of the braincase is pushed anteriorly and superiorly so that a part of the left parietal bone lies on top of the left frontal bone near a break along the coronal suture (Fig. 1C).

The mandible of DIK-1-1 was reconstructed by mirror-imaging: First, the better-preserved condyle process of the left side was mirrored to reconstruct the right side. Then, we symmetrized the lower jaw by mirror-imaging the reconstructed right side. To reconstruct the DIK-1-1 cranium, we first mirror-imaged the right frontal bone fragment as well as the right supraorbital region so as to replace the damaged left orbit. We then occluded the symmetrized mandible with the right side of the maxilla and restored the midline by translating and rotating the entire lower face together with the mandible. We then corrected for the slight displacement of the bone fragments of the nasal region, the orbital roof, the left zygomatic bone, and the maxilla. Next, we translated and rotated the braincase fragments of the left side posterior to the coronal suture. In the left lateral view, the lower face was subsequently rotated counterclockwise together with the mandible until the left mandibular condyle fit into the mandibular fossa of the repositioned left temporal bone. We mirror-imaged the repositioned left cranial base and aligned the bone fragments of the right temporal and occipital bone, respectively. Last, we repositioned the displaced basioccipital. We created multiple alternative reconstructions of DIK-1-1. These reconstructions were only subtly different as the exceptional preservation of the fossil bones together with the low degree of plastic distortion constrained the degrees of freedom. These multiple reconstructions were used to estimate a range of EVs.

Reconstruction of A.L. 333-105

The CT data of the *A. afarensis* infant A.L. 333-105 (Fig. 1, H to K) were first separated into individual fragments using manual segmentation along gaps and cracks (Fig. 1, L and N). We then repositioned these fragments based on anatomical criteria. First, we corrected the displacement of the superior part of the fronto-sphenoidal process of the right zygomatic bone and aligned this now complete zygomatic bone together with the zygomatic process of the right temporal to the right maxilla along the zygomatico-maxillary suture. The maxilla is broken exactly along the intermaxillary suture. We therefore used the maxilla to define a symmetry plane (*S*) and completed the lower face by mirror-imaging. The mirror-imaged right pterygoid processes almost perfectly overlap with the preserved pterygoid plates of the left side, indicating only a slight taphonomic displacement of the bones forming the left middle cranial fossa. Using the center of the left pterygoid fossa as a pivoting point and the coronal suture as a guide, we then repositioned the fragments of the left parietal and temporal bone so that the preserved portion of the zygomatic process of the left temporal aligns with the mirror-imaged zygomatic arch from the right side. The entire frontal bone is displaced and distorted, but on its inner table, the crista frontalis and impression created by the superior sagittal sinus make it possible to identify the midsagittal plane. Translating and rotating the frontal bone, we aligned its local midsagittal plane to *S* and mirrored the better-preserved right side. Next, the fragments of the left frontal bone and sphenoid bone were repositioned along the coronal suture. We then mirrored the left parietal and temporal across *S* to the right side. We created multiple anatomical reconstructions of the fossil and used these to compute a range of EVs (310 to 317 ml).

Estimation of EVs

EVs of the *A. afarensis* specimens were estimated using geometric morphometric methods based on measurement following the protocols described in (*40*, *41*) using Avizo, Edgewarp3D, and Mathematica. We used two different approaches to estimate EV in *A. afarensis*: (i) A thin-plate spline (TPS) prediction of missing data based on

endocranial measurements of complete ape crania. To this end, we measured a total of 935 anatomical landmarks and semilandmarks on CT scans of complete African ape crania (total $N = 122$; *Gorilla gorilla*, $N = 70$; *P. troglodytes*, $N = 52$) (*42*), as well as on the fossil reconstructions (Figs. 1 and 2) in Avizo. In Edgewarp3D, the semilandmarks were then allowed to slide iteratively on tangents to curves and surfaces so as to minimize the TPS bending energy between the respective fossil reconstructions and each reference specimen, and projected back onto the surface. This sliding step establishes geometric correspondence between the semilandmarks on the reference and target specimens (*43*, *44*). This algorithm yields 122 endocranial reconstructions for each of the following incomplete fossil specimens: DIK-1-1, A.L. 288-1, A.L. 444-2, and A.L. 822-1. For all reconstructions, we computed an EV following (*40*, *41*) to assess the reconstruction uncertainty. (ii) We also scaled each of the 122 endocranial reconstructions of the two most complete skulls (A.L. 822-1 and A.L. 444-2) to the less complete crania using a Procrustes fit based on a subset of the available endocranial landmarks and semilandmarks. This was done because the TPS approach based on ape endocrania may not accurately predict endocranial shape features specific to *A. afarensis* in A.L. 288-1 and A.L. 333-45. For A.L. 288-1, both algorithms predict very similar EVs: The mean EV is 391 ml (SD, 11 ml; range, 365 to 417 ml) using the TPS-based algorithm, and the scaling of A.L. 822-1 yields a mean EV of 385 ml (SD, 4 ml; range, 367 to 394 ml). For A.L. 288-1, we pooled the predictions of approaches (i) and (ii) in Table 1. When the EV of A.L. 333-45 is estimated by scaling different reconstructions of A.L. 444-2 based on the available landmarks and semilandmarks, the estimated mean EV is 488 ml (SD, 1 ml; range, 486 to 492 ml). As the entire frontal bone is missing in A.L. 333-45 and the TPS-based algorithm likely underestimates the true EV (TPS-based prediction: mean EV, 405 ml; SD, 5 ml; range, 395 to 417 ml), we report the more plausible EV estimates predicted by approach (ii) in Table 1.

Brain growth trajectories

The endocranial growth curves for chimpanzees and humans (Fig. 5) are based on published datasets (*5*, *6*, *11*, *26*, *40*, *42*, *45*–*52*) of EVs and brain weights comprising postmortem specimens ranging from birth to adulthood. Brain masses were converted to EVs following (*53*). We aimed to include as many specimens of known age as possible; specimens for which the calendar age at the time of death was not available were aged on the basis of their dentition (*54*). To visualize the average species growth trajectories, we computed Gompertz curves (Fig. 5, B to E) for chimpanzees and humans in Mathematica. For the computation of the Gompertz curves, the age of all individuals older than 11 was set to 11. In Fig. 5C, the black bar shows the entire rEV range of *A. afarensis* around 2.4 years of age (based on the age at death of DIK-1-1 and the similarity to A.L. 333-105), comparing the smallest EV estimation of DIK-1-1 to the largest estimate for A.L. 444-2 and the largest EV of A.L. 333-105 to the smallest adult EV (i.e., the smallest EV estimation of A.L. 288-1). Red dots represent average EVs of DIK-1-1 and A.L. 333-105 divided by the average EV of a random sample of adult *A. afarensis* drawn from the distribution of hundreds of EV estimates. In Fig. 5 (D and E), the red dots represent multiple EV comparisons of DIK-1-1 (rEV range, 52 to 76%; shown as a black bar) and A.L. 333-105 (rEV range, 59 to 87%; shown as a black bar), respectively, to one adult *A. afarensis* specimen (randomly sampled from the distribution of EV reconstructions). The two clusters at the lower end of the range correspond to comparisons with the large presumed male specimens A.L. 333-45 and A.L. 444-2. It has been argued that there is an evolutionary temporal trend within *A. afarensis* toward larger cranial size (*55*). When the large EV estimates of A.L. 444-2 are removed because this specimen is geologically younger than either infants (*32*), the average adult *A. afarensis* EV is 420 ml (SD, 49 ml; range, 365 to 492 ml). The observation that the *A. afarensis* growth trajectory indicates prolonged brain growth remains true when the large EV of A.L. 444-2 is removed from the computation and when the smaller TPS-based EV estimations are used for A.L. 333-45.

Brain organization

The identification and labeling of the sulcal impressions are as follows (*56*): C, sulcus centralis; fs, frontalis superior; fm, frontalis medius; fi, frontalis inferior; fo, fronto-orbitalis; h, horizontal ramus of pci; ip, s. intraparietalis; pci, praecentralis inferior; pcs, praecentralis superior; ps, parietalis superior; pti, postcentralis inferior; ptm, postcentralis medius; pts, postcentralis superior; L, S. lunatus; ts, temporalis superior; ts-a, ramus temporalis superior; tm, temporalis medius; occi, occipitalis inferior; lc, s. calcarinus lateralis; u, s. calcarinus ramus superior.

The chimpanzee's brain surface in Fig. 3 is based on a magnetic resonance image (MRI; turbo T2 weighting, voxel size of 0.438 mm). In Avizo, we first aligned the MRI to the CT scan of the same specimen and then used the CT endocast as a mask to extract the brain from the MRI; subsequently, we segmented the gyri manually. The modern human brain shown in figs. S1 and S4 is the "Colin 27 template," which combines a series of T1-weighted MR scans of a single subject with voxel sizes of 1 and 0.78 mm, respectively. The manual segmentation according to the Desikan-Killiany-Tourville cortical labeling protocol is from the Mindboggle-101 database (*57*).

Figure S4 illustrates the overall brain organization of a chimpanzee and a human in the left and right side of DIK-1-1 braincase, respectively. This figure makes it therefore possible to assess whether the position of the lunate sulcus in DIK-1-1 is ape-like or human-like. We used TPS interpolation based on the 935 anatomical landmarks and semilandmarks (the same as for the TPS warping of the endocranial surface described above) to warp the brain surfaces of the chimpanzee and the human to the cranial shape of the DIK-1-1 reconstruction. No endocranial landmarks defined by gyri and sulci were used for the TPS warps. The DIK-1-1 endocast has a clear and unambiguous impression of a lunate sulcus (shown as a yellow dotted line in fig. S4A) that is ape-like in both morphology and position. The lunate sulcus impression of the DIK-1-1 endocast falls exactly where it would be expected for a juvenile chimpanzee (fig. S4B). The identification of the sulcal impressions surrounding the lunate sulcus on the parietal and occipital and the lambdoidal suture corroborates this assessment.

SUPPLEMENTARY MATERIALS

Supplementary material for this article is available at http://advances.sciencemag.org/cgi/content/full/6/14/eaaz4729/DC1

View/request a protocol for this paper from *Bio-protocol*.

REFERENCES AND NOTES

1. S. R. Leigh, Brain growth, life history, and cognition in primate and human evolution. *Am. J. Primatol.* **62**, 139–164 (2004).
2. Z. Cofran, Brain size growth in Australopithecus. *J. Hum. Evol.* **130**, 72–82 (2019).
3. S. C. McFarlin, S. K. Barks, M. W. Tocheri, J. S. Massey, A. B. Eriksen, K. A. Fawcett, T. S. Stoinski, P. R. Hof, T. G. Bromage, A. Mudakikwa, M. R. Cranfield, C. C. Sherwood,

Early brain growth cessation in wild virunga mountain gorillas (*Gorilla beringei beringei*). *Am. J. Primatol.* **75**, 450–463 (2013).
4. S. L. Robson, B. Wood, Hominin life history: Reconstruction and evolution. *J. Anat.* **212**, 394–425 (2008).
5. J. J. Hublin, S. Neubauer, P. Gunz, Brain ontogeny and life history in Pleistocene hominins. *Philos. Trans. R Soc. Lond. B Biol. Sci.* **370**, 20140062 (2015).
6. H. Coqueugniot, J.-J. Hublin, F. Veillon, F. Houët, T. Jacob, Early brain growth in Homo erectus and implications for cognitive ability. *Nature* **431**, 299–302 (2004).
7. T. Sakai, A. Mikami, M. Tomonaga, M. Matsui, J. Suzuki, Y. Hamada, M. Tanaka, T. Miyabe-Nishiwaki, H. Makishima, M. Nakatsukasa, T. Matsuzawa, Differential prefrontal white matter development in chimpanzees and humans. *Curr. Biol.* **22**, 171 (2012).
8. E. Armstrong, K. Zilles, M. Curtis, A. Schleicher, Cortical folding, the lunate sulcus and the evolution of the human brain. *J. Hum. Evol.* **20**, 341–348 (1991).
9. A. A. de Sousa, C. C. Sherwood, H. Mohlberg, K. Amunts, A. Schleicher, C. E. MacLeod, P. R. Hof, H. Frahm, K. Zilles, Hominoid visual brain structure volumes and the position of the lunate sulcus. *J. Hum. Evol.* **58**, 281–292 (2010).
10. R. L. Holloway, D. Broadfield, M. S. Yuan, *The Human Fossil Record, Brain Endocasts—The Paleoneurological Evidence*, J. H. Schwartz, I. Tattersall, Eds. (John Wiley & Sons, 2004), vol. 3.
11. Z. Alemseged, F. Spoor, W. H. Kimbel, R. Bobe, D. Geraads, D. Reed, J. G. Wynn, A juvenile early hominin skeleton from Dikika, Ethiopia. *Nature* **443**, 296–301 (2006).
12. Z. Cofran, J. M. DeSilva, A neonatal perspective on *Homo erectus* brain growth. *J. Hum. Evol.* **81**, 41–47 (2015).
13. R. L. Holloway, Cerebral brain endocast pattern of *Australopithecus afarensis* hominid. *Nature* **303**, 420–422 (1983).
14. S. R. Leigh, Brain ontogeny and life history in Homo erectus. *J. Hum. Evol.* **50**, 104–108 (2006).
15. D. Falk, Hadar AL 162-28 endocast as evidence that brain enlargement preceded cortical reorganization in hominid evolution. *Nature* **313**, 45–47 (1985).
16. R. L. Holloway, W. H. Kimbel, Endocast morphology of Hadar hominid AL 162-28. *Nature* **321**, 536 (1986).
17. D. Falk, Endocast morphology of Hadar hominid AL 162-28—Reply. *Nature* **321**, 536–537 (1986).
18. D. Falk, C. P. E. Zollikofer, M. Ponce de León, K. Semendeferi, J. L. Alatorre Warren, W. D. Hopkins, Identification of in vivo sulci on the external surface of eight adult chimpanzee brains: Implications for interpreting early hominin endocasts. *Brain Behav. Evol.* **91**, 45–58 (2018).
19. R. L. Holloway, S. D. Hurst, H. M. Garvin, P. T. Schoenemann, W. B. Vanti, L. R. Berger, J. Hawks, Endocast morphology of Homo naledi from the Dinaledi Chamber, South Africa. *Proc. Natl. Acad. Sci. U.S.A.* **115**, 5738–5743 (2018).
20. R. L. Holloway, Revisiting the South African Taung australopithecine endocast: The position of the lunate sulcus as determined by the stereoplotting technique. *Am. J. Phys. Anthropol.* **56**, 43–58 (1981).
21. W. H. Kimbel, Y. Rak, The cranial base of Australopithecus afarensis: New insights from the female skull. *Philos. Trans. R Soc. Lond. B Biol. Sci.* **365**, 3365–3376 (2010).
22. A. Le Cabec, N. Tang, P. Tafforeau, Accessing developmental information of fossil hominin teeth using new synchrotron microtomography-based visualization techniques of dental surfaces and interfaces. *PLOS ONE* **10**, e0123019 (2015).
23. T. M. Smith, P. Tafforeau, A. L. Cabec, A. Bonnin, A. Houssaye, J. Pouech, J. Moggi-Cecchi, F. Manthi, C. Ward, M. Makaremi, C. G. Menter, Dental ontogeny in pliocene and early pleistocene hominins. *PLOS ONE* **10**, e0118118 (2015).
24. J. M. DeSilva, A shift toward birthing relatively large infants early in human evolution. *Proc. Natl. Acad. Sci. U.S.A.* **108**, 1022–1027 (2011).
25. K. Rosenberg, W. Trevathan, Birth, obstetrics and human evolution. *BJOG* **109**, 1199–1206 (2002).
26. J. M. DeSilva, J. J. Lesnik, Brain size at birth throughout human evolution: A new method for estimating neonatal brain size in hominins. *J. Hum. Evol.* **55**, 1064–1074 (2008).
27. R. G. Tague, C. O. Lovejoy, AL 288-1—Lucy or Lucifer: Gender confusion in the Pliocene. *J. Hum. Evol.* **35**, 75–94 (1998).
28. J. M. Desilva, N. M. Laudicina, K. R. Rosenberg, W. R. Trevathan, Neonatal Shoulder Width Suggests a Semirotational, Oblique Birth Mechanism in Australopithecus afarensis. *Anat. Rec.* **300**, 890–899 (2017).
29. H. M. Dunsworth, A. G. Warrener, T. Deacon, P. T. Ellison, H. Pontzer, Metabolic hypothesis for human altriciality. *Proc. Natl. Acad. Sci. U.S.A.* **109**, 15212–15216 (2012).
30. M. E. Pereira, S. R. Leigh, Modes of primate developement, in *Primate Life Histories and Socioecology*, P. M. Kappeler, M. E. Pereira, Eds. (University of Chicago Press, 2003), pp. 149–176.
31. K. Isler, C. P. van Schaik, Allomaternal care, life history and brain size evolution in mammals. *J. Hum. Evol.* **63**, 52–63 (2012).
32. W. H. Kimbel, Y. Rak, D. C. Johanson, *The Skull of* Australopithecus afarensis (Human Evolution Series, Oxford Univ. Press, 2004).
33. W. H. Kimbel, D. C. Johanson, Y. Coppens, Pliocene hominid cranial remains from the Hadar Formation, Ethiopia. *Am. J. Phys. Anthropol.* **57**, 453–499 (1982).
34. W. H. Kimbel, L. K. Delezene, "Lucy" redux: A review of research on australopithecus afarensis. *Am. J. Phys. Anthropol.* **140**, 2–48 (2009).
35. P. Gunz, P. Mitteroecker, S. Neubauer, G. W. Weber, F. L. Bookstein, Principles for the virtual reconstruction of hominin crania. *J. Hum. Evol.* **57**, 48–62 (2009).
36. K. J. Carlson, D. Stout, T. Jashashvili, D. J. de Ruiter, P. Tafforeau, K. Carlson, L. R. Berger, The endocast of MH1, *Australopithecus sediba*. *Science* **333**, 1402–1407 (2011).
37. T. M. Smith, P. Tafforeau, D. J. Reid, J. Pouech, V. Lazzari, J. P. Zermeno, D. Guatelli-Steinberg, A. J. Olejniczak, A. Hoffman, J. Radovčić, M. Makaremi, M. Toussaint, C. Stringer, J.-J. Hublin, Dental evidence for ontogenetic differences between modern humans and Neanderthals. *Proc. Natl. Acad. Sci. U.S.A.* **107**, 20923–20928 (2010).
38. K. L. Kuykendall, Dental development in chimpanzees (*Pan troglodytes*): The timing of tooth calcification stages. *Am. J. Phys. Anthropol.* **99**, 135–157 (1996).
39. R. S. Lacruz, M. C. Dean, F. Ramirez-Rozzi, T. G. Bromage, Megadontia, striae periodicity and patterns of enamel secretion in Plio-Pleistocene fossil hominins. *J. Anat.* **213**, 148–158 (2008).
40. F. Spoor, P. Gunz, S. Neubauer, S. Stelzer, N. Scott, A. Kwekason, M. C. Dean, Reconstructed *Homo habilis* type OH 7 suggests deep-rooted species diversity in early *Homo*. *Nature* **519**, 83–86 (2015).
41. S. Neubauer, P. Gunz, G. W. Weber, J. J. Hublin, Endocranial volume of *Australopithecus africanus*: New CT-based estimates and the effects of missing data and small sample size. *J. Hum. Evol.* **62**, 498–510 (2012).
42. S. Neubauer, J. J. Hublin, P. Gunz, The evolution of modern human brain shape. *Sci. Adv.* **4**, eaao5961 (2018).
43. P. Gunz, P. Mitteroecker, F. L. Bookstein, Semilandmarks in three dimensions, in *Modern Morphometrics in Physical Anthropology, Developments in Primatol: Progress and Prospect*, D. E. Slice, Ed. (Kluwer Academic/Plenum Publishers, 2005), pp. 73–98.
44. P. Gunz, P. Mitteroecker, Semilandmarks: A method for quantifying curves and surfaces. *Hystrix* **24**, 103–109 (2013).
45. N. Scott, S. Neubauer, J. J. Hublin, P. Gunz, A shared pattern of postnatal endocranial development in extant hominoids. *Evol. Biol.* **41**, 572–594 (2014).
46. S. Neubauer, P. Gunz, U. Schwarz, J.-J. Hublin, C. Boesch, Brief communication: Endocranial volumes in an ontogenetic sample of chimpanzees from the Taï Forest National Park, Ivory Coast. *Am. J. Phys. Anthropol.* **147**, 319–325 (2012).
47. S. Neubauer, P. Gunz, J.-J. Hublin, The pattern of endocranial ontogenetic shape changes in humans. *J. Anat.* **215**, 240–255 (2009).
48. J. G. Herndon, J. Tigges, D. C. Anderson, S. A. Klumpp, H. M. Mcclure, Brain weight throughout the life span of the chimpanzee. *J. Comp. Neurol.* **409**, 567–572 (1999).
49. J. DeSilva, J. Lesnik, Chimpanzee neonatal brain size: Implications for brain growth in *Homo erectus*. *J. Hum. Evol.* **51**, 207–212 (2006).
50. A. H. Schultz, The relative size of the cranial capacity in primates. *Am. J. Phys. Anthropol.* **28**, 273–287 (1941).
51. K. Isler, E. Christopher Kirk, J. M. A. Miller, G. A. Albrecht, B. R. Gelvin, R. D. Martin, Endocranial volumes of primate species: Scaling analyses using a comprehensive and reliable data set. *J. Hum. Evol.* **55**, 967–978 (2008).
52. F. Marchand, *Über das Hirngewicht des Menschen* (B.G. Teubner, 1902).
53. S. M. Blinkov, I. I. Glezer, *The Human Brain in Figures and Tables: A Quantitative Handbook* (Plenum Press and Basic Books, 1968).
54. C. Dean, B. Wood, in *Digital Archives of Human Paleobiology*, L. Bondioli, R. Macchiarelli, Eds. (Consiglio Nazionale delle Ricerche, ADS Solutions, 2003).
55. C. A. Lockwood, W. H. Kimbel, D. C. Johanson, Temporal trends and metric variation in the mandibles and dentition of *Australopithecus afarensis*. *J. Hum. Evol.* **39**, 23–55 (2000).
56. C. J. Conolly, *External Morphology of the Primate Brain* (Charles C. Thomas, 1950).
57. A. Klein, J. Tourville, 101 labeled brain images and a consistent human cortical labeling protocol. *Front. Neurosci.* **6**, 171 (2012).
58. A. Gómez-Robles, W. D. Hopkins, C. C. Sherwood, Modular structure facilitates mosaic evolution of the brain in chimpanzees and humans. *Nat. Commun.* **5**, 4469 (2014).
59. A. Gómez-Robles, W. D. Hopkins, S. J. Schapiro, C. C. Sherwood, Relaxed genetic control of cortical organization in human brains compared with chimpanzees. *Proc. Natl. Acad. Sci. U.S.A.* **112**, 14799–14804 (2015).
60. R. S. Lacruz, F. V. Ramirez Rozzi, Molar crown development in *Australopithecus afarensis*. *J. Hum. Evol.* **58**, 201–206 (2010).
61. T. M. Smith, P. Tafforeau, D. J. Reid, R. Grün, S. Eggins, M. Boutakiout, J.-J. Hublin, Earliest evidence of modern human life history in North African early *Homo sapiens*. *Proc. Natl. Acad. Sci. U.S.A.* **104**, 6128–6133 (2007).
62. J.-C. Labiche, O. Mathon, S. Pascarelli, M. A. Newton, G. G. Ferre, C. Curfs, G. Vaughan, A. Homs, D. F. Carreiras, Invited article: The fast readout low noise camera as a versatile x-ray detector for time resolved dispersive extended x-ray absorption fine structure and diffraction studies of dynamic problems in materials science, chemistry, and catalysis. *Rev. Sci. Instrum.* **78**, 091301 (2007).

63. D. Paganin, S. C. Mayo, T. E. Gureyev, P. R. Miller, S. W. Wilkins, Simultaneous phase and amplitude extraction from a single defocused image of a homogeneous object. *J. Microsc.* **206**, 33–40 (2002).
64. S. Sanchez, P. E. Ahlberg, K. M. Trinajstic, A. Mirone, P. Tafforeau, Three-dimensional synchrotron virtual paleohistology: A new insight into the world of fossil bone microstructures. *Microsc. Microanal.* **18**, 1095–1105 (2012).

Acknowledgments: We thank the Authority for Research and Conservation of Cultural Heritage and the National Museum of Ethiopia of the Ministry of Culture and Tourism, and the musée des Confluences (Lyon, France) for access to specimens and permission to conduct the scanning. We are indebted to Y. Desta, T. Getachew, M. Endalemaw, and Y. Assefa for facilitating scanning in Addis Ababa. We are grateful to A. Barash, J.-J. Hublin, M. C. Dean, N. Jeffery, T. Preuss, J. Rilling, A. Stoessel, R. David, H. Temming, and D. Plotzki for help with aspects of this study. **Funding:** Research was supported by the Max Planck Society (P.G., S.N., A.L.C., and F.S.; Evolution of Brain Connectomics to P.G.), the ESRF (ec597 to F.S., Z.A., and P.T.), U.S. NSF (BCS 1126470 to T.M.S. and P.T.), M. and W. Hearst (Z.A.), and the Institute of Human Origins at Arizona State University (W.H.K.). **Author contributions:** All authors collected original fossils and/or measurement data, contributed to the interpretation of the results, and edited the manuscript. Z.A. and W.H.K. directed field work at Dikika and Hadar. P.T., F.S., Z.A., and W.H.K. scanned original fossils. P.G. and S.N. segmented CT and MRI scans and developed analytical methods. P.G. created fossil reconstructions, performed analyses, and designed figures with contributions from S.N. Sulcal imprints on endocasts were analyzed by D.F., S.N., and P.G. Fossil and extant endocrania were measured by S.N., who also estimated EVs. P.T., A.L.C., F.S., and Z.A. scored dental ages. P.T., A.L.C., and T.M.S. analyzed dentition of infant fossils and developed methods for age at death estimation. A.L.C. and P.T. analyzed the synchrotron CT data of the DIK-1-1 dentition. P.G. wrote the manuscript with contributions from all authors. **Competing interests:** The authors declare that they have no competing interests. **Data and materials availability:** All data needed to evaluate the conclusions in the paper are present in the paper and/or the Supplementary Materials.

Submitted 11 September 2019
Accepted 9 January 2020
Published 1 April 2020
10.1126/sciadv.aaz4729

Citation: P. Gunz, S. Neubauer, D. Falk, P. Tafforeau, A. Le Cabec, T. M. Smith, W. H. Kimbel, F. Spoor, Z. Alemseged, *Australopithecus afarensis* endocasts suggest ape-like brain organization and prolonged brain growth. *Sci. Adv.* **6**, eaaz4729 (2020).

Australopithecus afarensis endocasts suggest ape-like brain organization and prolonged brain growth

Philipp Gunz, Simon Neubauer, Dean Falk, Paul Tafforeau, Adeline Le Cabec, Tanya M. Smith, William H. Kimbel, Fred Spoor and Zeresenay Alemseged

Sci Adv **6** (14), eaaz4729.
DOI: 10.1126/sciadv.aaz4729